

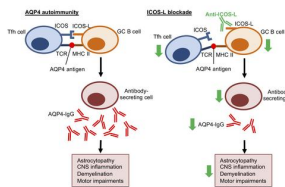
T follicular helper cells contribute to pathophysiology in a model of neuromyelitis optica spectrum disorders

Leung-Wah Yick, ... , Jason Shing-Cheong Kwan, Koon-Ho Chan

JCI Insight. 2023. <https://doi.org/10.1172/jci.insight.161003>.

Research In-Press Preview Neuroscience

Graphical abstract



Find the latest version:

<https://jci.me/161003/pdf>



Title:

T follicular helper cells contribute to pathophysiology in a model of neuromyelitis optica spectrum disorders

Authors:

Leung-Wah Yick,^{1,2} Oscar Ka-Fai Ma,^{1,2} Ethel Yin-Ying Chan,^{1,2} Krystal Xiwing Yau,^{1,2}
Jason Shing-Cheong Kwan,^{1,2} and Koon-Ho Chan^{1,2}

Authors' affiliations:

¹Department of Medicine, Li Ka Shing Faculty of Medicine, The University of Hong Kong, Hong Kong, China.

²Neuroimmunology and Neuroinflammation Research Laboratory, Li Ka Shing Faculty of Medicine, The University of Hong Kong, Hong Kong, China.

Corresponding author: Koon-Ho Chan, MD, PhD

Department of Medicine, Li Ka Shing Faculty of Medicine, The University of Hong Kong, 4/F, Professorial Block, Queen Mary Hospital, 102 Pokfulam Road, Hong Kong, China.

Tel: (852) 2255 3595; Email: koonho@hku.hk

Conflict-of-interest statement:

LWY, OKFM, EYYC, KXY and JSCK declare no competing interests. KHC has received research funding support from Merck Pharmaceutical Ltd., Novartis Pharmaceutical Ltd., Bayer HealthCare Ltd., honorarium for invited lectures and chairmanship from Biogen Idec Ltd., UCB Pharma Ltd., Merck Pharmaceutical Ltd., Sanofi-Aventis Hong Kong Ltd., Eli Lilly Asia, Inc. (Hong Kong), Eisai (Hong Kong) Co. Ltd., and sponsorship to attend conferences from Novartis Pharmaceutical Ltd., Bayer HealthCare Ltd., UCB Pharma Ltd., Merck Pharmaceutical Ltd., Sanofi-Aventis Hong Kong Ltd., and Eisai (Hong Kong) Co. Ltd.

Abstract:

Neuromyelitis optica spectrum disorders (NMOSD) are inflammatory autoimmune disorders of the CNS. Immunoglobulin G autoantibodies targeting the aquaporin-4 water channel (AQP4-IgG) are the pathogenic effector of NMOSD. Dysregulated T follicular helper (Tfh) cells have been implicated in the loss of B-cell tolerance in autoimmune diseases. The contribution of Tfh cells to disease activity and the therapeutic potential of targeting these cells in NMOSD remain unclear. Here, we established an autoimmune model of NMOSD by immunizing mice against AQP4 via *in vivo* electroporation. After AQP4 immunization, mice displayed AQP4 autoantibodies in the blood circulation, blood-brain barrier disruption, and IgG infiltration in the spinal cord parenchyma. Moreover, AQP4 immunization induced motor impairments and NMOSD-like pathologies including astrocytopathy, demyelination, axonal loss, and microglia activation. These were associated with increased splenic Tfh, T helper 1 (Th1) and T helper 17 (Th17) cells, memory B cells, and plasma cells. *Aqp4*-deficient mice did not display motor impairments and NMOSD-like pathologies after AQP4 immunization. Importantly, abrogating inducible costimulator (ICOS)/inducible costimulator ligand (ICOS-L) signalling using anti-ICOS-L antibody depleted Tfh cells and suppressed the response of Th1 and Th17 cells, memory B cells, and plasma cells in AQP4-immunized mice. These findings were associated with ameliorated motor impairments and spinal cord pathologies. This study suggests a role of Tfh cells in the pathophysiology of NMOSD in a novel mouse model with AQP4 autoimmunity. It also provides an animal model for further investigating the immunological mechanisms underlying AQP4 autoimmunity, and for developing novel therapeutic interventions targeting the autoimmune reactions in NMOSD.

Introduction

Neuromyelitis optica spectrum disorders (NMOSD) are severe inflammatory demyelinating disorders of the CNS clinically characterized by optic neuritis, myelitis, and encephalitis (1). Most NMOSD patients are seropositive for immunoglobulin G (IgG) autoantibodies targeting the water channel aquaporin-4 (AQP4) (2, 3), which is highly expressed on the membrane of astrocyte endfeet. AQP4-IgG are directly pathogenic, and NMOSD patients seropositive for these autoantibodies have underlying AQP4 autoimmunity (4). Less is known about the immunological mechanisms underlying AQP4-IgG production, although loss of B cell tolerance has been suggested to be a contributing factor. In the CNS, the binding of AQP4-IgG to astrocytic AQP4 leads to the development of NMOSD pathologies including astrocytopathy, glutamate excitotoxicity, blood-brain barrier (BBB) disruption, neuroinflammation, demyelination, and neuronal injury (5–10).

The generation of AQP4-specific autoreactive B cells has been suggested to be a consequence of impaired immunological tolerance (11). In an *ex vivo* study of B cell subsets derived from NMOSD patients, the production of AQP4-specific antibody-secreting B cells was promoted by a culture condition that mimicked T-cell help (12). T follicular helper (Tfh) cells are critical for the differentiation of B cells into memory B cells, plasmablast, and plasma cells that produce isotype-switched, high-affinity antibodies (13). They are characterized by high-level expression of CXC chemokine receptor type 5 (CXCR5), programmed cell death protein 1 (PD1), and inducible costimulator (ICOS) (13).

Tfh-cell differentiation occurs in secondary lymphoid organs including lymph nodes and the spleen. In the T-cell zone, dendritic cells present antigen and costimulatory signals to naïve T-helper cells. Then pre-Tfh cells migrate to the T-B cell border, where they receive antigen

presentation and ICOS-ligand (ICOS-L) costimulation from antigen-specific B cells. Fully differentiated Tfh cells migrate to germinal centres (GC). They form cognate interactions with GC B cells, and secrete interleukin-21 (IL-21), IL-4, CD40L, and CXCL13 to support B-cell survival and differentiation into antibody-secreting cells. Notably, sustained ICOS/ICOS-L signalling is needed for early T-cell activation, Tfh-cell differentiation and migration, as well as Tfh-cell phenotype maintenance. The idea of disrupting the interaction between Tfh cells and B cells to remove potentially pathogenic B cells has received significant attention in the field of autoimmune diseases (14). Recent studies have found a correlation between the expansion of circulating Tfh cells and the disease activity in NMOSD patients (15–18). However, the contribution of Tfh cells to immunopathogenesis and the therapeutic potential of targeting the ICOS/ICOS-L signalling pathway in NMOSD remain unclear.

Reported animal models of NMOSD are based on passive transfer of purified IgG from AQP4-IgG seropositive patients or recombinant AQP4 antibodies to rodents (19–26). We recently showed that intraperitoneal injection of human AQP4-IgG induced motor impairments and NMOSD-like CNS pathologies in mice (27, 28). While these models are able to demonstrate the pathological effects of AQP4-IgG, they fail to recapitulate the autoimmunity underlying NMOSD with production of AQP4 autoantibodies. Here, we developed a mouse model of NMOSD with AQP4 autoimmunity using electroporation-mediated immunization. These mice displayed the production of IgG autoantibodies against AQP4 in blood circulation, and this was associated with motor impairments and NMOSD-like CNS pathologies. Importantly, the disease activity of these mice was reversed by suppressing Tfh-cell response via blockade of ICOS/ICOS-L signalling pathway.

Results

In vivo electroporation induces AQP4 overexpression in skeletal muscle

The M23 isoform of AQP4 exists in the plasma membrane as homotetrameric and heterotetrameric units, which aggregate to form intramembranous particles (IMPs) and high order orthogonal arrays of particles (OAPs) (29, 30). To transfect the tibialis anterior muscle of each mouse, we employed *in vivo* electroporation with a plasmid encoding the M23 isoform of mouse AQP4 (pAQP4) and an empty plasmid vector control (pEmpty). The distribution of AQP4 in muscle fibres after electroporation was visualized by immunostaining. The muscle from naïve mice showed weak and diffuse distribution of AQP4 immunoreactivity and no Myc-DDK staining. The muscle from the mice that received pEmpty showed weak AQP4 immunoreactivity but strong Myc-DDK staining. Electroporation with pAQP4 increased the number and fluorescent intensity of AQP4 and Myc-DDK co-stained muscle fibres with punctate distribution of immunoreactivity suggestive of OAP lattices ($P < 0.001$; Figure 1B and D). Transfection of HEK293 cells with pAQP4 followed by immunostaining confirmed that AQP4 was expressed on the membrane of the transfected cells with an OAP lattice-like structure (Supplemental Figure 1). Haematoxylin and eosin (H&E) staining revealed prominent necrotic inflammation in the muscle following electroporation as characterized by marked immune cell infiltration ($P < 0.001$; Figure 1C and E).

To characterize AQP4 expression in tibialis anterior muscle after electroporation, we performed BN-PAGE to separate the native forms of AQP4 tetramers, IMPs and OAPs. Immunoblot analysis revealed that electroporation with pAQP4 profoundly increased the expression of M23 tetramers, IMPs and OAPs in the muscle compared to naïve and pEmpty controls (Figure 1F, upper panel). Next, we resolved denatured proteins from the muscle by

SDS-PAGE. Immunoblot analysis revealed that electroporation with pAQP4 robustly increased the expression of a 60 kDa fusion protein, which represents AQP4 monomers together with Myc-DDK, in the muscle compared to naïve and pEmpty controls (Figure 1F, lower panel). These findings indicate that electroporation with pAQP4 induces the overexpression of AQP4 M23 isoform and triggers inflammation in mouse skeletal muscle.

AQP4 immunization generates circulating AQP4 autoantibodies

We have shown that cell-based indirect immunofluorescence assay using transfected HEK293 cells expressing human AQP4 on the cell membrane is sensitive and specific for the detection of AQP4-IgG in NMOSD patients (31). To detect AQP4 autoantibodies in mouse serum after AQP4 immunization, we performed the same assay but used transfected HEK293 cells expressing the mouse AQP4 M23 isoform. Signal was visualized by mouse IgG-specific fluorescent-conjugated secondary antibody. In the positive control using commercial anti-AQP4 antibody to stain the transfected cells, we found positive AQP4 immunoreactivity on the membrane of the cells. In the negative controls, which neither commercial anti-AQP4 antibody was added nor the cells were transfected, no AQP4 immunoreactivity was observed (Figure 2A, upper panel). Moreover, there was no AQP4 immunoreactivity detected when the serum of naïve, pEmpty(C/P+), and pAQP4(C/P-) mice was used to stain the cells. However, positive AQP4 immunoreactivity was observed when the serum of pAQP4(C/P+) mice was used (Figure 2A, lower panel). These results indicate that the serum of pAQP4(C/P+) mice contain autoantibodies that recognize the M23 isoform of mouse AQP4, including its conformational epitopes.

To determine the titre of AQP4 autoantibodies, the serum of mice in different groups was analysed using competitive ELISA. No AQP4 autoantibodies were detected in the serum of

naïve and pEmpty mice. A low titre of AQP4 autoantibodies was found in the serum of pAQP4(C/P-) mice. By contrast, the serum of pAQP4(C/P+) mice displayed a higher titre of AQP4 autoantibodies (Figure 2B). Using serum diluted in 1:1000, the concentration of AQP4 autoantibodies in pAQP4(C/P+) mice was significantly higher than that in naïve, pEmpty(C/P+), and pAQP4(C/P-) mice ($P < 0.001$; Figure 2C). These results support that AQP4 immunization via in vivo electroporation triggers the production of AQP4 autoantibodies in mouse circulation.

AQP4 is predominantly located on the astrocytic foot processes at the BBB (32). Next, we tested whether the serum from AQP4-immunized mice could immunostain the spinal cord sections that were obtained from wild-type and *Aqp4*-deficient (*Aqp4*^{-/-}) mice. There was no detectable immunoreactivity when the serum of pEmpty(C/P+) mice was used to stain the spinal cord sections from wild-type mice and *Aqp4*^{-/-} mice. However, when the serum of pAQP4(C/P+) mice was used, positive staining was found at the blood vessels of the spinal cord from wild-type mice, but not at that from *Aqp4*^{-/-} mice (Figure 2D). These results further confirm that AQP4-immunized mice contain circulating AQP4 autoantibodies.

AQP4 immunization induces motor impairments

Clinical signs of encephalomyelitis were assessed by experimental autoimmune encephalomyelitis (EAE) score. From day 0 to day 42, pAQP4(C/P+) mice did not display motor weakness compared to naïve, pEmpty(C/P+) and pAQP4(C/P-) mice (score 0, data not shown). At day 42, we examined whether AQP4 immunization led to motor impairments using beam walking test. pAQP4(C/P+) mice took longer time to cross a 1.2 x 80 cm (width x length) beam than naïve, pEmpty(C/P+) and pAQP4(C/P-) mice ($P < 0.001$, Figure 3A). During the beam walking test, pAQP4(C/P+) mice slipped more often than control mice ($P <$

0.05; Figure 3B). Similar findings were observed when the test was performed with a narrower 0.6 x 80 cm beam. pAQP4(C/P+) mice took longer time ($P < 0.001$; Figure 3C) and slipped more often ($P < 0.01$; Figure 3D) than controls. These results indicate that AQP4-immunized mice displayed motor impairments.

Circulating AQP4 autoantibodies infiltrate the spinal cord

Without passing through the BBB, circulating AQP4-IgG in the peripheral blood do not cause CNS damage and acute attack in NMOSD (24). To disrupt the BBB in this model, mice were injected with CFA and PTx before electroporation as described previously (27, 33). At day 42, immunostaining for the tight junction protein ZO-1 revealed a continuous staining pattern in the spinal cord blood vessels of naïve and pAQP4(C/P-) mice, but a discontinuous pattern in that of pEmpty(C/P+) and pAQP4(C/P+) mice (Figure 4A). These results indicate that CFA and PTx injections can disrupt the BBB.

Next, we investigated whether circulating AQP4 autoantibodies generated by AQP4 immunization infiltrated the spinal cord after BBB disruption. Mouse IgG immunoreactivity was found in the spinal cord parenchyma of pAQP4(C/P+) mice, but not in that of controls (Figure 4B and D). Co-immunostaining confirmed that these mouse IgG targeted AQP4 in the spinal cord (Supplemental Figure 2). These findings confirm that circulating AQP4 autoantibodies infiltrate the spinal cord through a disrupted BBB.

AQP4 immunization induces astrocytopathy

A hallmark histopathological feature of NMOSD lesions is astrocytopathy characterized by prominent loss of AQP4 and GFAP (34). We assessed whether AQP4 immunization induces astrocytopathy in our model. Co-immunostaining revealed profound decrease in AQP4 and

GFAP levels in the spinal cord of pAQP4(C/P+) mice compared to naïve, pEmpty(C/P+) and pAQP4(C/P-) mice (Figure 4C). Merging of the images showed that the loss of AQP4 colocalized with the loss of GFAP immunoreactivity (Figure 4C). Quantification of immunofluorescence intensity confirmed significant reduction in AQP4 and GFAP levels in pAQP4(C/P+) mice ($P < 0.001$; Figure 4E and F). Similar results were observed in the optic nerve of mice in different groups (Supplemental Figure 3A, C and D). These data suggest that AQP4 autoantibodies generated by AQP4 immunization cause astrocytopathy in mouse CNS.

AQP4 immunization induces demyelination and axonal loss

Next, we assessed the effect of AQP4 immunization on demyelination, which is another histopathological feature of NMOSD lesions (34). The spinal cord of pAQP4(C/P+) mice displayed patchy loss of Olig2 (oligodendrocyte marker; Figure 5A) and MBP (myelin marker; Figure 5B) immunoreactivities, while this loss was not observed in naïve, pEmpty(C/P+) and pAQP4(C/P-) mice. Quantification of immunofluorescence intensity showed significant decrease in Olig2 ($P < 0.001$; Figure 5E) and MBP ($P < 0.001$; Figure 5F) levels in pAQP4(C/P+) mice. Luxol fast blue staining confirmed that demyelination occurred in the spinal cord of pAQP4(C/P+) mice, but not in that of controls (Supplemental Figure 4A).

We further examined axonal loss after AQP4 immunization using NF-H as an axonal marker. NF-H-positive spots in the spinal cord of pAQP4(C/P+) mice were less dense than that of controls (Figure 5C). Counting of NF-H spots confirmed significant axonal loss in pAQP4(C/P+) mice ($P < 0.001$; Figure 5G). Co-immunofluorescence of MBP and NF-H revealed an association of demyelination with axonal loss (Figure 5D). These findings were also observed in the optic nerve of mice in different groups (Supplemental Figure 3B, E and

F). Fluorescent Nissl staining did not show any loss of motoneurons in the ventral horn and interneurons around the central canal in the spinal cord of pAQP4(C/P+) mice (Supplemental Figure 4B and C). Taken together, these results indicate that AQP4 immunization leads to demyelination and axonal loss.

AQP4 immunization activates microglia

Prominent microglia activation has been found in the lesion of NMOSD patients and previous experimental models of NMOSD (10, 22, 23, 28, 35). In the present model, we examined whether astrocytopathy, demyelination, and axonal loss coincide with microglia activation. We used Iba-1 as a monocyte marker that labels both brain-derived microglia and infiltrated macrophages. The spinal cord of pAQP4(C/P+) mice displayed marked increase in Iba-1 immunoreactivity compared to naïve, pEmpty(C/P+) and pAQP4(C/P-) mice (Figure 6A). Quantification of immunofluorescence intensity confirmed significant increase in Iba-1 level in pAQP4(C/P+) mice ($P < 0.001$) (Figure 6B). Co-immunostaining of Iba-1 and GFAP revealed that activated microglia were in close proximity to astrocytes (Figure 6C).

Activated microglia release excessive proinflammatory cytokines, including tumour necrosis factor- α (TNF- α), interleukin-1 β (IL-1 β), and interleukin-6 (IL-6), to mediate neuroinflammation (36). To assess the level of these cytokines in our model, ELISA was performed in the spinal cord homogenate of mice in different groups. The level of TNF- α , IL-1 β and IL-6 in pAQP4(C/P+) mice was significantly higher than that in naïve, pEmpty(C/P+) and pAQP4(C/P-) mice ($P < 0.001$) (Figure 6D-F). These results suggest a role of microglia activation in the development of NMOSD-like lesion in AQP4-immunized mice.

Complement activation and immune cell infiltration in AQP4-immunized mice

Next, we assessed whether AQP4 immunization induces complement complex deposition and immune cell infiltration. C5b-9 (terminal complement complex marker) immunoreactivity was observed in the spinal cord of pAQP4(C/P+) mice, but not in that of naïve, pEmpty(C/P+) and pAQP4(C/P-) mice (Supplemental Figure 5A). Scattered Ly6G (neutrophil marker) and Siglec-F (eosinophil marker) immunoreactive cells were found in the spinal cord of pAQP4(C/P+) mice, but not in that of controls (Supplemental Figure 5B and C).

CD68-immunoreactive cells, which represented both brain-derived and infiltrated macrophages, were observed in the spinal cord of pAQP4(C/P+) mice, but not in that of controls (Supplemental Figure 5D). However, sparse F4/80-immunoreactive cells, which represented infiltrated macrophages, were found in the spinal cord of pAQP4(C/P+) mice (Supplemental Figure 5E). These results suggest that only a few circulating macrophages infiltrated the spinal cord parenchyma.

H&E staining confirmed prominent immune cell infiltration in the spinal cord of pAQP4(C/P+) mice (Supplemental Figure 5F). We did not find any immunoreactivity for CD49b (natural killer cells), CD19 (B cells), and CD4 (T helper cells) in the spinal cord of mice in all groups (data not shown).

Aqp4^{-/-} mice do not display NMOSD-like disease activity after AQP4 immunization

To confirm this experimental disease model is mediated by an autoimmune reaction to AQP4, we performed AQP4 immunization in *Aqp4^{-/-}* mice and wild-type littermate controls. Beam walking test revealed that wild-type pAQP4(C/P+) mice took longer time to cross a 1.2 x 80

cm (width x length) beam than *Aqp4*^{-/-} pAQP4(C/P+) mice ($P < 0.001$, Figure 7A). Wild-type pAQP4(C/P+) mice slipped more often than *Aqp4*^{-/-} pAQP4(C/P+) mice ($P < 0.001$; Figure 7B). Similar findings were observed when the test was performed with a 0.6 x 80 cm beam (Figure 7C and D). Next, we examined whether *Aqp4*^{-/-} mice displayed NMOSD-like pathologies after AQP4 immunization. As expected, the spinal cord of *Aqp4*^{-/-} pAQP4(C/P+) mice did not show any AQP4 immunoreactivity. Importantly, there was significant difference in GFAP immunoreactivity between the spinal cord of *Aqp4*^{-/-} pAQP4(C/P+) and wild-type pAQP4(C/P+) mice ($P < 0.001$; Figure 7E and F). Moreover, the spinal cord of *Aqp4*^{-/-} pAQP4(C/P+) mice displayed profound reduction in Iba-1 immunoreactivity compared to wild-type pAQP4(C/P+) mice ($P < 0.001$; Figure 7G and H). There were no patchy loss of MBP immunoreactivity and decrease in the number of NF-H spots in *Aqp4*^{-/-} pAQP4(C/P+) mice compared to wild-type pAQP4(C/P+) mice ($P < 0.001$; Figure 7I and J). These results indicate that the motor impairments and NMOSD-like pathologies observed in this model are driven by an autoimmune response against AQP4, hence they are not observed in immunized *Aqp4*^{-/-} mice.

AQP4 immunization induces the expansion of splenic Tfh, Th1, Th17, memory B cells, and plasma cells

Tfh cells drive GC responses with B-cell proliferation, differentiation, isotype switching, somatic hypermutation, and affinity maturation (13). In NMOSD patients, the frequency of circulating Tfh cells has been found to be correlated with the disease activity (15–18). Consistently, we did not find any difference in the circulating Tfh-cell frequency between healthy controls (HC) and NMOSD patients in remission receiving immunosuppressive therapy (Supplemental Table 1 and Supplemental Figure 6). In the present animal model, we observed increase in the frequency of Tfh cells (CD4⁺CXCR5⁺PD-1⁺, $P < 0.001$;

Supplemental Figure 7A and D), Th1 cells ($CD4^+IFN\gamma^+$, $P < 0.001$; Supplemental Figure 7B and E), Th17 cells ($CD4^+IL-17A^+$, $P < 0.001$; Supplemental Figure 7C and F), memory B cells ($CD19^+CD80^+$, $P < 0.05$; Supplemental Figure 8A and C), and plasma cells ($CD19^-CD138^+TACI^+$, $P < 0.05$; Supplemental Figure 8B and D) in the spleen of pAQP4(C/P+) mice compared to naïve, pEmpty(C/P+) and pAQP4(C/P-) mice.

Anti-ICOS-L antibody ameliorates disease activity in AQP4-immunized mice

Tfh cells require a sustained ICOS/ICOS-L signalling to maintain their phenotype (37, 38). Abrogation of the signalling with antibodies targeting ICOS or ICOS-L has been shown to deplete Tfh cells and suppress GC responses (37, 38). To examine whether Tfh cells influence B-cell responses, we depleted Tfh cells in pAQP4(C/P+) mice using anti-ICOS-L antibody (Figure 8A). We found that anti-ICOS-L antibody-treated pAQP4(C/P+) mice had fewer splenic Tfh-cells than isotype control antibody-treated pAQP4(C/P+) mice ($CD4^+CXCR5^+PD-1^+$, $P < 0.001$; Figure 8B). Moreover, the frequency of splenic Th1 cells ($CD4^+IFN\gamma^+$, $P < 0.01$; Figure 8C), Th17 cells ($CD4^+IL-17A^+$, $P < 0.001$; Figure 8D), memory B cells ($CD19^+CD80^+$, $P < 0.01$; Figure 8E), and plasma cells ($CD19^-CD138^+TACI^+$, $P < 0.01$; Figure 8F) in anti-ICOS-L antibody-treated pAQP4(C/P+) mice was significantly lower than that in controls.

Next, we investigated whether anti-ICOS-L antibody treatment ameliorates NMOSD-like disease activity in AQP4-immunized mice. Beam walking test revealed that anti-ICOS-L antibody-treated pAQP4(C/P+) mice took shorter time to cross the 1.2 x 80 cm and 0.6 x 80 cm beams than isotype control antibody-treated pAQP4(C/P+) mice ($P < 0.05$; Figure 9A and B). During the walking test on the 0.6 x 80 cm beam, anti-ICOS-L antibody-treated mice slipped less often than control ($P < 0.05$; Figure 9B). Consistent with improved motor

functions, there were less AQP4 and GFAP losses in the spinal cord of anti-ICOS-L antibody-treated pAQP4(C/P+) mice compared to controls (Figure 9C). Quantification of immunofluorescence intensity confirmed that these reductions were significant ($P < 0.05$; Figure 9E). Furthermore, anti-ICOS-L antibody treatment prevented loss of MBP immunoreactivity and NF-H spots in the spinal cord of pAQP4(C/P+) mice compared to controls (Figure 9D). Quantification of MBP immunofluorescence intensity and number of NF-H spots confirmed that these observations were significant (MBP, $P < 0.01$; NF-H, $P < 0.05$; Figure 9F). Taken together, these results suggest that Tfh-cell depletion via the abrogation of ICOS/ICOS-L signalling prevents AQP4 immunization-induced motor impairments and NMOSD-like pathologies.

Discussion

In this study, we demonstrated that AQP4 immunization via *in vivo* electroporation triggered an autoimmune response that produces autoantibodies against AQP4 in mice. These autoantibodies infiltrated the spinal cord and bound to the AQP4 on astrocytes. AQP4-immunized mice displayed motor impairments and NMOSD-like pathologies including astrogliopathy, demyelination, axonal loss, and microglia activation. These motor impairments and pathologies were not observed in *Aqp4*-deficient mice after AQP4 immunization. Using this model, we demonstrated that the depletion of Tfh cells by abrogating ICOS/ICOS-L signalling ameliorates NMOSD-like disease activity. Our study provides a novel mouse model of NMOSD with AQP4 autoimmunity in which Tfh cells contribute to its pathophysiology. This model can be used in future studies to elucidate the autoimmune mechanisms underlying the production of AQP4 autoantibodies and to evaluate novel immune cell-targeted therapeutic interventions for NMOSD.

Electroporation-mediated immunization triggers both humoral and cellular immune responses, resulting in the generation of antibodies against the native conformation of a protein-of-interest in vivo (39, 40). Skeletal muscle is a suitable site for electroporation because it is composed of a large volume of easily accessible post-mitotic cells, which allow long-term and stable expression of the transfected gene (41). Square-wave electric pulses enhance the transfection efficiency and expression level of a target protein by folds (40, 42). In addition, electric pulses cause damage and inflammation in muscle, resulting in a recruitment of immune cells to the immunization site and the development of immunological memory (39). Pre-treatment of skeletal muscle with cardiotoxin before electroporation accelerates antibody production through the recruitment of antigen-presenting cells (40). In pAQP4(C/P-) mice, we detected a low titre of AQP4 antibodies by ELISA, but not by cell-based assay. These mice might contain AQP4 autoantibodies targeting linear epitopes of mouse AQP4 at a low titre. On the contrary, in pAQP4(C/P+) mice, we detected autoantibodies that bound to mouse AQP4 by both ELISA and cell-based assay. These findings suggest that AQP4 immunization induces an AQP4-specific autoimmune response. It generates autoantibodies targeting linear and conformational epitopes of AQP4. In the present work, we sought to use electroporation-mediated immunization to trigger the production of autoantibodies against self-AQP4 in mice. Therefore, we used a plasmid that encodes the mouse AQP4. It is possible that immunization using a plasmid encoding AQP4 of other species could produce a stronger immune response and a higher titre of AQP4 antibodies than using the mouse AQP4 plasmid. Previous studies found that immunization with recombinant AQP4 protein or peptides could not induce motor impairments and CNS pathologies in mice (1, 43). NMOSD-like lesions were achieved by co-injection of AQP4-IgG and human complement into the brain and by systemic injection of AQP4-IgG into rodents with disrupted BBB (20, 21, 44, 45). The discrepancy in the findings between these

studies and ours suggests that electroporation-mediated immunization is a more efficient method to drive pathogenic AQP4 autoimmunity in rodents.

We found that AQP4-immunized mice displayed signs of motor impairments. This observation is consistent with those from previous murine models, in which AQP4-IgG from NMOSD patients were delivered by intracerebral injection (21), intrathecal injection (23), intraventricular infusion (24), or intraperitoneal injection (27). This suggests that the AQP4 autoantibodies produced in our model can lead to clinical motor impairments reminiscent of human AQP4-IgG.

A pathological hallmark of NMOSD is astrocytopathy in the spinal cord and optic nerves, characterized by AQP4 and GFAP losses (1). Various experimental animal models have attempted to recapitulate astrocytopathy in human NMOSD by passive transfer of human AQP4-IgG or AQP4-sensitized T cells to rodents (46). Findings from these models suggest that the binding of AQP4-IgG to astrocytic AQP4 activates the classical complement system, leading to astrocytic loss that is mediated by complement-dependent cytotoxicity (CDC) (5, 21, 22, 47–49). Interestingly, the presence of serum complement inhibitor CD59 has been suggested to limit the classical complement activity in mouse (50, 51). On the contrary, another study showed that CD59 is broadly expressed in peripheral organs of mouse, while its expression is restricted in the brain (52). Following AQP4 immunization, we observed that AQP4 and GFAP losses coincided with C5b-9 deposition. The binding of AQP4 autoantibodies on astrocytic membrane may aggregate the AQP4 M23 isoform to produce OAPs that activate complements (53, 54). Further studies should investigate the role of intrinsic complement inhibitors in lesion development and disease progression in our model. Another mechanism of astrocytopathy in NMOSD has been suggested to involve antibody-

dependent cell-mediated cytotoxicity (ADCC). This is triggered by the binding of Fc-gamma receptors on myeloid cells to the Fc portion of astrocyte-bound AQP4 autoantibodies, leading to the release of cytotoxic compounds and the phagocytosis of astrocytes (55–58). We recently reported that passive transfer of AQP4-IgG from NMOSD patients to mice induced profound astrocytopathy that was likely mediated by ADCC (27). Here, we observed prominent microglia activation together with neutrophil and eosinophil infiltration in the spinal cord of AQP4-immunized mice. Moreover, activated microglia were in close proximity to astrocytes. Consistent with previous findings, our data further support existing evidence that the astrocytopathy in NMOSD is partly mediated by ADCC.

We found that AQP4-immunized mice displayed prominent oligodendrocyte loss, demyelination, and axonal loss. Oligodendrocytes and neurons do not express AQP4, therefore they are not directly damaged by AQP4-IgG (21). Recent studies have highlighted a complement bystander mechanism that mediates secondary oligodendrocyte and neuronal damage in NMOSD. It involves a local diffusion of activated complements following the binding of AQP4-IgG to astrocytes, resulting in a deposition of membrane attack complex on neighbouring oligodendrocytes and neurons (59, 60). Moreover, the secondary damage has been suggested to involve a complement-independent ADCC bystander mechanism (58). This mechanism is mediated by activated microglia and myeloid cells that undergo phagocytosis and produce pro-inflammatory cytokines and oxidative metabolites (58, 61–63). Most recently, the evolving NMOSD pathophysiology induced by AQP4-IgG infusion in mice has been shown to be dependent on the interaction between astrocytes and microglia that involves a microglial C3a receptor signalling (64). In the present model, oligodendrocyte loss, demyelination, and axonal loss coincided with microglia activation, increased pro-inflammatory cytokine levels, terminal complement complex deposition, and granulocyte

infiltration. These lesion features are consistent with those from previous studies. Taken together, these findings indicate that the binding of AQP4-IgG to astrocytes triggers secondary myelin and neuronal damage that is mediated by complex local inflammatory responses. Our model provides a perspective for further studies on the pathophysiology involved following the binding of AQP4-IgG to astrocytic AQP4.

Our study suggests that Tfh cells contribute to the pathophysiology of NMOSD-like disease in a mouse model with AQP4 autoimmunity induced by AQP4 immunization. Abrogating ICOS/ICOS-L signalling suppressed Tfh-cell expansion, reduced Th1-, Th17-, memory B- and plasma cell responses, as well as ameliorated motor impairments and NMOSD-like pathologies in AQP4-immunized mice. No significant difference was found in the frequency of circulating Tfh cells between healthy controls and NMOSD patients in remission receiving immunosuppressive therapy. These findings are consistent with recent clinical studies of circulating Tfh cells in NMOSD patients. The frequency of circulating Tfh cells during relapse was higher than that during remission, and decrease in the proportion of Tfh cells by methylprednisolone treatment was associated with relapse prevention in NMOSD patients (15). Circulating Tfh cell and B cell frequencies also closely correlated with the disease activity of NMOSD, and depletion of IL-6-producing B cells inhibited circulating Tfh cell expansion (16, 17). Untreated NMOSD patients displayed a Tfh polarization toward excessive B-helper Tfh subsets, which was restored by B-cell depletion therapy (18). These findings support the hypothesis that dysregulated Tfh cells favour B-cell differentiation and AQP4-IgG production. To our knowledge, this present model is the first animal model with AQP4 autoimmunity that mimics T-cell responses in NMOSD. In EAE, a widely used animal model of multiple sclerosis, Tfh-cell frequency in the CNS was found to be increased during peak of the disease (65). The number of infiltrating Tfh cells was correlated with that of

infiltrating B cells; and adoptive transfer of Tfh cells increased severity and delayed remission (66). Blocking the infiltration of Tfh cells using anti-CXCL13 antibody alleviated the disease (67). These findings indicate a role of Tfh cells in the pathogenesis of autoimmune neuroinflammation. Future studies on T- and B-cell interactions using the present model may provide a better understanding on the autoimmune mechanisms leading to AQP4-IgG production. Moreover, future experiments on examining the effects of interventions known to suppress NMOSD can add validity to the present model and to the targeting of Tfh cells. Indeed, we planned to examine whether B-cell suppression alleviates disease and the associated shift in B- and T-cell phenotypic profiles using this model in a future study.

A limitation of this study is that we examined the production of AQP4 autoantibodies and NMOSD-like pathologies following AQP4 immunization at one time point only. Further studies are needed to investigate whether AQP4 immunization generates Tfh cells that precede GC expansion. It would also be important to examine the long-term effects of AQP4 immunization on NMOSD-like disease activity in this model. Additionally, Th1, Th17 and T follicular regulatory cells express ICOS, although its expression is highest on GC Tfh cells (14). We cannot exclude the possibility that the effect of anti-ICOS-L antibody observed here was partly influenced by other T-cell subsets.

In summary, we demonstrate that AQP4 immunization via electroporation triggers AQP4 autoantibody production that is associated with motor impairments, NMOSD-like pathologies, and increase in splenic Tfh, Th1, Th17, memory B and plasma cells in mice. Moreover, our results suggest that modulating ICOS/ICOS-L signalling affects Tfh cells which contribute to the pathophysiology in this novel NMOSD model. Future studies on the

precise role of T- and B-cell subsets in AQP4 autoantibody production and disease severity can extrapolate this model to further understanding of NMOSD pathogenesis. This model may also be useful for evaluating novel therapies for the disease.

Methods

NMOSD patients

Samples were obtained from 4 healthy controls (HC) and 6 NMOSD patients enrolled at the Department of Medicine, Queen Mary Hospital, Hong Kong, from June to November 2022. For NMOSD patients, inclusion criteria were age ≥ 18 years, a diagnosis of AQP4-IgG-seropositive NMOSD according to the 2015 International Panel for NMO Diagnosis (IPND) consensus criteria (68), and no matter the disease course and disease modifying treatment. Exclusion criteria were another immune disorder, infection or cancer. AQP4-IgG serostatus was assessed using cell-based indirect immunofluorescence assay in our hospital as reported previously (31). Age, gender, disease duration, current treatment, and relapse/remission status were recorded. Degree of disability was assessed by neurological examination with Expanded Disability Status Scale (EDSS) score. None of the HC had a history of disease or infection and none received any treatment during the previous 2 months. Written informed consent was obtained from all subjects.

Animals

Female wild-type C57BL/6N mice (The Jackson Laboratory) of age 6 to 8 weeks were housed in our animal facilities at Centre for Comparative Medicine Research, The University of Hong Kong. *Aqp4*^{-/-} mice were obtained from Cyagen and were housed under specific pathogen-free conditions. Animals were kept in groups of four to five per cage under a 12 h dark/light cycle and provided with free access to water and chow.

Plasmids

Plasmid encoding the mouse AQP4 M23 isoform (pAQP4) and empty vector control (pEmpty) were obtained from OriGene. The pAQP4 plasmid contained mouse AQP4 cDNA inserted into Myc-DDK-tagged expression vector with cytomegalovirus (CMV) promoter. Plasmids were transformed and amplified in *Escherichia coli* competent cells (Clontech). The integrity of the constructs produced was confirmed by DNA sequencing analysis. Plasmid DNA for in vivo electroporation was prepared by Plasmid Purification Maxi Kit (Qiagen) according to manufacturer's instructions. The quantity and quality of DNA were assessed by optical density at 260 and 280 nm.

AQP4 immunization via electroporation

The procedure of animal experiment is summarized in Figure 1A. AQP4 immunization via in vivo electroporation was performed as described previously with modifications (40). At 7 days before the first electroporation, under anaesthesia with ketamine (100 mg/kg) and xylazine (10 mg/kg), mice were injected with 10 μ M in 50 μ l of cardiotoxin (Latoxan) at the right tibialis anterior muscle. Then they received four subcutaneous injections of 50 μ l complete Freund's adjuvant (CFA, BD Biosciences) containing 50 μ g heat killed H37Ra *Mycobacterium tuberculosis* (Difco) at four sites on the hind flank, two at shoulder and two at lower back. In addition, mice received intraperitoneal injections (i.p.) of pertussis toxin (PTx, 200 ng in 200 μ l PBS, List Biological Laboratories) at 7 and 3 days before the first electroporation.

At day 0, under anaesthesia, mice received an intramuscular injection of either pEmpty control or pAQP4 (50 μ g DNA in 35 μ l PBS) into the right tibialis anterior muscle using

Hamilton syringe (Postnova Analytics). Immediately after DNA injection, square wave electric pulses (8 pulses of 100 V/cm, duration 20 ms, and frequency 1.0 Hz) generated by an electroporator (ECM830, BTX) were delivered to the muscle using a pair of calliper electrodes (BTX). The electroporation procedure was repeated at days 14 and 28.

Naïve mice without receiving any treatments were served as normal control. We termed pEmpty(C/P+) mice as the mice that received pEmpty electroporation and treated with CFA and PTx; pAQP4(C/P-) mice as those that received pAQP4 but without CFA and PTx; and pAQP4(C/P+) mice as those that received both pAQP4 electroporation and CFA and PTx treatment. Each group contained eight mice.

Treatment with anti-ICOS-L antibody

Tfh cells were depleted using a blockade of ICOS/ICOS-L signalling as described previously (38). Beginning at day 0, AQP4-immunized mice were administered with 150 µg in 200 µl PBS of anti-ICOS-L (Clone HK5.3, BioXCell) or isotype control (Clone 2A3, BioXCell) antibody via i.p. injection every other day for 42 days (Figure 8A).

Motor assessments

All motor assessments were assessed by a researcher blinded to the experimental conditions. Motor weakness of mice was assessed by EAE score as described previously (27, 33). From day 0 to day 42, mice were weighted and examined daily on a six-grade scale: 0 = no clinical signs; 1 = weight loss, limp tip of tail; 2 = limp tail, mild paraparesis; 3 = moderate paraparesis, ataxia; 4 = tetraparesis; 5 = moribund. Mice would be culled if they had weight loss exceeding 20-30% of initial body weight or developed severe weakness (score 4-5).

At day 42, motor impairments of mice were detected by beam walking test (69). This test examined the animal's ability to keep upright and walk across an elevated narrow beam to a platform. The apparatus consisted of two 80 cm-long beams with a width of 1.2 and 0.6 cm, resting 50 cm above a table top on two stands. The time for the mouse to cross each beam and the number of paw slips during the process were recorded.

Serum collection and tissue harvesting

After beam walking test, mice were euthanized with an excessive dose of ketamine and xylazine. Blood samples were harvested from the facial vein of the mice with animal lancets (Medipoint). Sera were obtained by collecting the supernatants after centrifuging the clotted blood samples at 6,000 rpm for 15 min at 4°C. Tibialis anterior muscles and cervical spinal cords were freshly dissected out, frozen in liquid nitrogen, and stored at -80°C. Some animals were perfused transcardially with ice-cold PBS, followed by 4% paraformaldehyde. Tibialis anterior muscles, cervical spinal cords and optic nerves were harvested, post-fixed with 4% paraformaldehyde, cryoprotected with 30% sucrose, and sectioned in 10 µm using cryostat.

BN-PAGE, SDS-PAGE, and immunoblotting

For BN-PAGE, muscle samples were homogenized by sonication in Native PAGE sample buffer containing 1% dodecyl-B-D-maltoside. Homogenates were centrifuged at 12,000 rpm for 10 min at 4°C. Supernatants were collected and protein concentrations were determined by DC assay (Bio-Rad). Homogenates (5 µg of protein each well) were mixed with 0.5% Coomassie G250 and subjected to 3-12% Bis-Tris gel electrophoresis with Native PAGE running buffer according to the manufacturer's instructions (Novex). Proteins were then transferred onto polyvinylidene fluoride (PVDF) membrane and fixed in 8% acetic acid. Membranes were rinsed with methanol to remove background dye.

For SDS-PAGE, muscle samples were homogenized by sonication in lysis buffer.

Homogenates were centrifuged at 12,000 g for 10 mins at 4°C. Supernatants were collected and protein concentrations were determined by DC assay (Bio-Rad). Homogenates (20 µg of protein each well) were electrophoresed in 10% SDS polyacrylamide gel. Proteins were transferred to PVDF membrane.

Next, membranes from BN-PAGE and SDS-PAGE were subjected to immunoblotting. Non-specific bindings of the blots were blocked with 5% non-fat dry milk in Tris Buffered Saline-Tween-20 (TBST). Blots were probed with rabbit anti-mouse AQP4 antibody (1:1000, catalog A5971, Sigma-Aldrich) at 4°C overnight, washed with TBST, and incubated with HRP-conjugated anti-rabbit antibody (1:5000, catalog P0448, Dako). After washing with TBST, signals were visualized by enhanced chemiluminescence (Advansta) using ChemiDoc Imaging system (Bio-Rad).

Cell-based indirect immunofluorescence assay

Cell-based indirect immunofluorescence assay was performed as described previously with modifications (31). Human embryonic kidney (HEK) 293 cells (ATCC) were seeded onto eight-well chamber slides at 10,000 cells/well and cultured in Dulbecco's Modified Eagle Medium (DMEM) in 5% CO₂ at 37°C. They were transfected with pAQP4 using Lipofectamine 3000 (Invitrogen) according to manufacturer's instructions. Cells were fixed with 4% paraformaldehyde, washed with PBS, and blocked with 1% bovine serum albumin (BSA) in PBS. Sera of mice were diluted at 1:10 with PBS containing 1% BSA.

Commercially available rabbit anti-mouse AQP4 antibody (catalog A5971, Sigma-Aldrich) was diluted at 1:500 and used as positive control. To remove non-specific antibodies, diluted

sera were incubated with rat liver powder at room temperature for 1 h and then centrifuged at 14,000 rpm for 15 mins. Next, 100 μ l of the diluted sera were added to each well and incubated at 4°C overnight. After washing with PBS, cells were incubated with either Alexa 488-conjugated anti-mouse IgG (for samples) (catalog A21202) or anti-rabbit IgG (for positive control) (catalog A11070) secondary antibody (all from Thermo Fisher Scientific) at room temperature for 1 h. Cells were coverslipped with antifade reagent containing DAPI (Thermo Fisher Scientific).

Immunostaining and histochemistry

Cryosections of tibialis anterior muscles were incubated with rabbit anti-mouse AQP4 (1:200, catalog A5971, Sigma-Aldrich) and mouse anti-DDK (FLAG, 1:500, catalog TA50011-100, OriGene) at 4°C overnight. Cryosections of spinal cords and optic nerves were incubated with the following primary antibodies at 4°C overnight: (1) rabbit anti-zonula occludens 1 (ZO-1, 1:200, catalog AB216880, Abcam), (2) goat anti-mouse IgG (1:100, catalog AB6708, Abcam), (3) rabbit anti-AQP4 (1:200, catalog A5971, Sigma-Aldrich), (4) mouse anti-gial fibrillary acidic protein (GFAP, 1:200, catalog SC33673, Santa Cruz Biotechnology), (5) rabbit anti-oligodendrocyte transcription factor 2 (Olig2, 1:200, catalog AB9610, Millipore), (6) goat anti-myelin basic protein (MBP, 1:200, catalog SC13914, Santa Cruz Biotechnology), and (7) rabbit anti-neurofilament (NF-H, 1:400, catalog N4142, Sigma-Aldrich), (8) rabbit anti-ionized calcium-binding adapter molecule 1 (Iba-1, 1:200, catalog 019-19741, Wako), (9) rabbit anti-terminal complement complex (C5b-9, 1:200, catalog AB55811, Abcam), (10) rat anti-lymphocyte antigen 6 complex locus G6D (Ly6G, 1:400, catalog AB2557, Abcam), (11) rat anti-Siglec-F (1:50, catalog 552125, BD Bioscience), (12) mouse anti-cluster of differentiation 68 (CD68, 1:200, catalog YM3161, Immunoway), (13) rat anti-F4/80 (1:200, catalog AB6640, Abcam). Sections were then incubated with the

appropriate Alexa-Fluor-conjugated secondary antibodies (Thermo Fisher Scientific) at room temperature for 1 h. Neuronal cells were visualized using blue fluorescent Nissl stain (NeuroTrace, Thermo Fisher Scientific). Sections were coverslipped with antifade reagent containing DAPI (Thermo Fisher Scientific). Selected sections were stained with H&E and Luxol fast blue using standard procedures.

Microscopy

All images were captured using the same microscope (Eclipse Ni, Nikon) and digitized with SPOT software 5.0 (Diagnostic Instruments). Signal intensity was quantified using ImageJ software (Version 1.53e, NIH).

ELISA

Titre of AQP4 antibodies in mice sera was determined using mouse anti-AQP4 competitive ELISA kit (catalog MBS746880, MyBioSource) according to manufacturer's instructions. Briefly, 96-well plates were pre-coated with AQP4. Sera from mice were added at serial dilutions from 1:10 to 1:10,000. Standards and samples were incubated with anti-AQP-HRP conjugate that competed for AQP4 antigen binding sites. After washing, colour was developed with horseradish peroxidase substrate and optical density was measured at 450 nm using microplate reader (CLARIO star, BMG Labtech).

Concentrations of TNF- α , IL-1 β , and IL-6 in spinal cord homogenates were assessed using mouse sandwich ELISA kits (TNF- α , catalog ELM-TNF α -CL-1) (IL-1 β , catalog ELM-IL1 β -CL-1) (IL-6, catalog ELM-IL6-CL-1) (all from RayBiotech) according to manufacturer's protocols. Briefly, standards and samples were added into 96-well plates pre-coated with anti-TNF- α , anti-IL-1 β or anti-IL-6 antibodies. After incubation, wells were washed and

biotinylated antibodies for mouse TNF- α , IL-1 β , and IL-6 were added accordingly. After washing, wells were added with HRP-conjugated streptavidin, washed, and then added with TMB substrate for colour development. The optical density of each well was measured at 450 nm using microplate reader (CLARIO star, BMG Labtech). Concentrations (pg/ml) of the cytokines were normalized with the total protein content of the samples (pg/mg protein).

Flow cytometry

Human

Blood samples from HC and NMOSD patients were collected in EDTA tubes. Peripheral blood mononuclear cells (PBMC) were isolated by diluting blood with RPMI 1640 medium (1:1) and layered over Ficoll-Paque PLUS density gradient medium (Cytiva) according to manufacturer's instruction. PBMC were incubated with an antibody cocktail containing anti-human CD4-FITC (catalog 556615), anti-human CXCR5-PerCP-Cy5.5 (catalog 562781), and anti-human PD-1-PE (catalog 560908) (all from BD Biosciences) at 4°C for 30 mins. Data were acquired using CytoFLEX flow cytometer (Beckman Coulter) and analysed using FlowJo software (Version 10.8, FlowJo).

Mice

Single-cell suspensions from the spleens of mice were isolated with 40 μ m cell strainers. Cells were incubated with antibody cocktails containing anti-mouse CD16/CD32 Fc block (catalog 553142, BD Biosciences) at 4°C for 30 mins. The antibodies were: anti-mouse CD4-FITC (catalog 553729), anti-mouse CXCR5-PE-Cy7 (catalog 560671), anti-mouse PD-1-PE (catalog 551892), anti-mouse IFN γ -PE (catalog 562020), anti-mouse IL-17A-PE (catalog 561020), anti-mouse CD19-V450 (catalog 560375), anti-mouse CD80-APC (catalog 560016), anti-mouse PD-L2-PE (catalog 557796), anti-mouse CD138-PE (catalog 561070),

and anti-mouse TACI-Alexa Fluor-647 (catalog 558453) (all from BD Biosciences). Data were acquired using CytoFLEX flow cytometer (Beckman Coulter) and analysed using FlowJo software (Version 10.8, FlowJo).

Statistics

Differences between groups were compared by one-way ANOVA with post hoc Tukey's test. The difference between two groups was determined by Student's *t* test. Calculations were performed using Prism 6 (GraphPad Software Inc). Data are shown as mean \pm SEM. Levels of significance are indicated with * $P < 0.05$, ** $P < 0.01$, and *** $P < 0.001$.

Study approval

The human study was approved by The University of Hong Kong/Hospital Authority Hong Kong West Cluster Institutional Review Board, Hong Kong. All animal experiments were approved by the Committee on the Use of Live Animals in Teaching and Research, The University of Hong Kong.

Author contributions

LWY and KHC conceived and designed the study. LWY, OKFM, and JSCK performed the experiments. EYYC contributed to the experiment on *Aqp4*^{-/-} mice. KXY organized patient visits and collected blood samples. LWY analyzed the data and wrote the manuscript. KHC gave comments on the manuscript. All authors revised and approved the manuscript.

Acknowledgements

This work was supported by CCL & YYS Private Donations for Research in Multiple Sclerosis and Related Disorders; Seed Fund for Basic Research, University Research

Committee, The University of Hong Kong; and Health & Medical Research Fund, Food and Health Bureau, Hong Kong (Project no. 09201006).

References

1. Hinson SR, Lennon VA, Pittock SJ. Autoimmune AQP4 channelopathies and neuromyelitis optica spectrum disorders. In: *Handbook of Clinical Neurology*. Elsevier; 2016:377–403
2. Lennon PVA et al. A serum autoantibody marker of neuromyelitis optica: Distinction from multiple sclerosis. *Lancet*. 2004;364(9451):2106–2112.
3. Jiao Y et al. Aquaporin 4 IgG serostatus and outcome in recurrent longitudinally extensive transverse myelitis. *JAMA Neurol*. 2014;71(1):48–54.
4. Pittock SJ, Lucchinetti CF. Neuromyelitis optica and the evolving spectrum of autoimmune aquaporin-4 channelopathies: A decade later. *Ann N Y Acad Sci*. 2016;1366:20–39.
5. Hinson SR, Pittock SJ, Lucchinetti CF. Pathogenic potential of IgG binding to water channel extracellular domain in neuromyelitis optica. *Neurology*. 2007;69:2221–2231.
6. Hinson SR et al. Aquaporin-4-binding autoantibodies in patients with neuromyelitis optica impair glutamate transport by down-regulating EAAT2. *J Exp Med*. 2008;205(11):2473–81.
7. Lucchinetti CF et al. A role for humoral mechanisms in the pathogenesis of Devic's neuromyelitis optica. *Brain*. 2002;125(7):1450–1461.
8. Papadopoulos MC, Verkman AS. Aquaporin 4 and neuromyelitis optica. *Lancet Neurology*. 2012;11(6):535–544.

9. Roemer SF et al. Pattern-specific loss of aquaporin-4 immunoreactivity distinguishes neuromyelitis optica from multiple sclerosis. *Brain*. 2007;130(5):1194–1205.
10. Misu T et al. Presence of six different lesion types suggests diverse mechanisms of tissue injury in neuromyelitis optica. *Acta Neuropathol*. 2013;125(6):815–827.
11. Cotzomi E et al. Early B cell tolerance defects in neuromyelitis optica favour anti-AQP4 autoantibody production. *Brain*. 2019;142(6):1598–1615.
12. Wilson R et al. Condition-dependent generation of aquaporin-4 antibodies from circulating B cells in neuromyelitis optica. *Brain*. 2018;1063–1074.
13. Crotty S. T follicular helper cell biology: A decade of discovery and diseases. *Immunity*. 2019;50(5):1132–1148.
14. Edner NM, Carlesso G, Rush JS, Walker LSK. Targeting co-stimulatory molecules in autoimmune disease. *Nat Rev Drug Discov*. 2020;19:860–883.
15. Li YJ et al. Association of circulating follicular helper T cells with disease course of NMO spectrum disorders. *J Neuroimmunol*. 2015;278:239–246.
16. Zhao C et al. Increased circulating T follicular helper cells are inhibited by rituximab in neuromyelitis optica spectrum disorder. *Front Neurol*. 2017;8:1–9.
17. Monteiro C et al. The expansion of circulating IL-6 and IL-17-secreting follicular helper T cells is associated with neurological disabilities in neuromyelitis optica spectrum disorders. *J Neuroimmunol*. 2019;330:12–18.
18. Nicolas P et al. The balance in T follicular helper cell subsets is altered in neuromyelitis optica spectrum disorder patients and restored by rituximab. *Front Immunol*. 2019;10:2826.

19. Bradl M, Lassmann H. Experimental models of neuromyelitis optica. *Brain Pathology*. 2014;24(1):74–82.
20. Kinoshita M et al. Anti-aquaporin-4 antibody induces astrocytic cytotoxicity in the absence of CNS antigen-specific T cells. *Biochem Biophys Res Commun*. 2010;394(1):205–210.
21. Saadoun S et al. Intra-cerebral injection of neuromyelitis optica immunoglobulin G and human complement produces neuromyelitis optica lesions in mice. *Brain*. 2010;133(2):349–361.
22. Asavapanumas N, Ratelade J, Verkman AS. Unique neuromyelitis optica pathology produced in naïve rats by intracerebral administration of NMO-IgG. *Acta Neuropathol*. 2014;127(4):539–551.
23. Geis C et al. The intrinsic pathogenic role of autoantibodies to aquaporin 4 mediating spinal cord disease in a rat passive-transfer model. *Exp Neurol*. 2015;265:8–21.
24. Marignier R et al. Neuromyelitis optica study model based on chronic infusion of autoantibodies in rat cerebrospinal fluid. *J Neuroinflammation*. 2016;13(1):111.
25. Felix CM, Levin MH, Verkman AS. Complement-independent retinal pathology produced by intravitreal injection of neuromyelitis optica immunoglobulin G. *J Neuroinflammation*. 2016;13(1):275.
26. Hillebrand S et al. Circulating AQP4-specific auto-antibodies alone can induce neuromyelitis optica spectrum disorder in the rat. *Acta Neuropathol*. 2019;137(3):467–485.
27. Yick LW, Ma OKF, Ng RCL, Kwan JSC, Chan KH. Aquaporin-4 autoantibodies from neuromyelitis optica spectrum disorder patients induce complement-independent immunopathologies in mice. *Front Immunol*. 2018;9:1438.

28. Yick LW, Tang CH, Ma OKF, Kwan JSC, Chan KH. Memantine ameliorates motor impairments and pathologies in a mouse model of neuromyelitis optica spectrum disorders. *J Neuroinflammation*. 2020;17(1):236.
29. Crane JM, Bennett JL, Verkman AS. Live cell analysis of aquaporin-4 M1/M23 interactions and regulated orthogonal array assembly in glial cells. *J Biol Chem*. 2009;284(51):35850–35860.
30. Iorio R et al. Astrocytic autoantibody of neuromyelitis optica (NMO-IgG) binds to aquaporin-4 extracellular loops, monomers, tetramers and high order arrays. *J Autoimmun*. 2013;40(1):21–27.
31. Chan KH et al. Aquaporin-4 autoantibodies in neuromyelitis optica spectrum disorders: comparison between tissue-based and cell-based indirect immunofluorescence assays. *J Neuroinflammation*. 2010;7:50.
32. Lennon VA, Kryzer TJ, Pittock SJ, Verkman AS, Hinson SR. IgG marker of optic-spinal multiple sclerosis binds to the aquaporin-4 water channel. *J Exp Med*. 2005;202(4):473–477.
33. Chan KH et al. Aquaporin-4 autoantibodies cause asymptomatic aquaporin-4 loss and activate astrocytes in mouse. *J Neuroimmunol*. 2012;245:32–8.
34. Lucchinetti CF et al. The pathology of an autoimmune astrocytopathy: Lessons learned from neuromyelitis optica. *Brain Pathology*. 2014;24(1):83–97.
35. Popescu BF et al. Neuromyelitis optica unique area postrema lesions: nausea, vomiting, and pathogenic implications. *Neurology*. 2011;76(14):1229–1237.
36. Colonna M, Butovsky O. Microglia Function in the Central Nervous System During Health and Neurodegeneration. *Annu Rev Immunol*. 2017;35(1):441–468.

37. Kim AR et al. Targeting inducible costimulator expressed on CXCR5+PD-1+ TH cells suppresses the progression of pemphigus vulgaris. *J Allergy Clin Immunol.* 2020;146(5):1070–1079.
38. Uwadiae FI, Pyle CJ, Walker SA, Lloyd CM, Harker JA. Targeting the ICOS/ICOS-L pathway in a mouse model of established allergic asthma disrupts T follicular helper cell responses and ameliorates disease. *Allergy.* 2019;74(4):650–662.
39. Rochard A, Scherman D, Bigey P. Genetic immunization with plasmid DNA mediated by electrotransfer. *Hum Gene Ther.* 2011;22(7):789–798.
40. Allard B et al. Electroporation-aided DNA immunization generates polyclonal antibodies against the native conformation of human endothelin B receptor. *DNA Cell Biol.* 2011;30(9):727–37.
41. Mir LM et al. High-efficiency gene transfer into skeletal muscle mediated by electric pulses. *Proc Natl Acad Sci USA.* 1999;96(8):4262–7.
42. Alexandrenne C et al. Electrotransfer of cDNA coding for a heterologous prion protein generates autoantibodies against native murine prion protein in wild-type mice. *DNA Cell Biol.* 2010;29(3):121–131.
43. Kalluri SR et al. Functional characterization of aquaporin-4 specific t cells: Towards a model for Neuromyelitis optica. *PLoS One.* 2011;6(1):e16083.
44. Bradl M et al. Neuromyelitis optica: Pathogenicity of patient immunoglobulin in vivo. *Ann Neurol.* 2009;66(5):630–643.
45. Kinoshita M et al. Neuromyelitis optica: Passive transfer to rats by human immunoglobulin. *Biochem Biophys Res Commun.* 2009;386(4):623–627.

46. Duan T, Verkman AS. Experimental animal models of aquaporin-4-IgG-seropositive neuromyelitis optica spectrum disorders: progress and shortcomings. *Brain Pathol.* 2020;30(1):13–25.
47. Phuan PW et al. C1q-targeted monoclonal antibody prevents complement-dependent cytotoxicity and neuropathology in in vitro and mouse models of neuromyelitis optica. *Acta Neuropathol.* 2013;125(6):829–840.
48. Zhang H, Bennett JL, Verkman AS. Ex vivo spinal cord slice model of neuromyelitis optica reveals novel immunopathogenic mechanisms. *Ann Neurol.* 2011;70(6):943–954.
49. Phuan PW, Ratelade J, Rossi A, Tradtrantip L, Verkman AS. Complement-dependent cytotoxicity in neuromyelitis optica requires aquaporin-4 protein assembly in orthogonal arrays. *J Biol Chem.* 2012;287(17):13829–13839.
50. Ratelade J, Verkman AS. Inhibitor(s) of the classical complement pathway in mouse serum limit the utility of mice as experimental models of neuromyelitis optica. *Mol Immunol.* 2014;62(1):104–113.
51. Zhang H, Verkman AS. Longitudinally extensive NMO spinal cord pathology produced by passive transfer of NMO-IgG in mice lacking complement inhibitor CD59. *J Autoimmun.* 2014;53(C):67–77.
52. Baalalubramanian S et al. CD59a is the primary regulator of membrane attack complex assembly in the mouse. *J Immunol.* 2004;173(6):3684–3692.
53. Hinson SR et al. Molecular outcomes of neuromyelitis optica (NMO)-IgG binding to aquaporin-4 in astrocytes. *Proc Natl Acad Sci USA.* 2012;109(4):1245–1250.
54. Soltys J et al. Membrane assembly of aquaporin-4 autoantibodies regulates classical complement activation in neuromyelitis optica. *J Clin Invest.* 2019;129(5):2000–2013.

55. Hertwig L et al. Distinct functionality of neutrophils in multiple sclerosis and neuromyelitis optica. *Mult Scler.* 2016;22(2):160–73.
56. Zhang H, Verkman AS. Eosinophil pathogenicity mechanisms and therapeutics in neuromyelitis optica. *J Clin Invest.* 2013;123(5):2306–2316.
57. Ratelade J et al. Involvement of antibody-dependent cell-mediated cytotoxicity in inflammatory demyelination in a mouse model of neuromyelitis optica. *Acta Neuropathol.* 2013;126(5):699–709.
58. Duan T, Smith AJ, Verkman AS. Complement-independent bystander injury in AQP4-IgG seropositive neuromyelitis optica produced by antibody-dependent cellular cytotoxicity. *Acta Neuropathol Commun.* 2019;7:1–16.
59. Duan T, Smith AJ, Verkman AS. Complement-dependent bystander injury to neurons in AQP4-IgG seropositive neuromyelitis optica. *J Neuroinflammation.* 2018;15(1):294.
60. Tradtrantip L, Yao X, Su T, Smith AJ, Verkman AS. Bystander mechanism for complement-initiated early oligodendrocyte injury in neuromyelitis optica. *Acta Neuropathol.* 2017;134(1):35–44.
61. Arimoto T, Bing G. Up-regulation of inducible nitric oxide synthase in the substantia nigra by lipopolysaccharide causes microglial activation and neurodegeneration. *Neurobiol Dis.* 2003;12(1):35–45.
62. Gyoneva S et al. Systemic inflammation regulates microglial responses to tissue damage in vivo. *Glia.* 2014;62(8):1345–1360.
63. West PK, Viengkhou B, Campbell IL, Hofer MJ. Microglia responses to interleukin-6 and type I interferons in neuroinflammatory disease. *Glia.* 2019;67(10):1821–1841.

64. Chen T et al. Astrocyte-microglia interaction drives evolving neuromyelitis optica lesion. *J Clin Invest.* 2020;130(8):4025–4038.
65. Baniahmad A et al. The frequency of follicular T helper cells differs in acute and chronic neuroinflammation. *Sci Rep.* 2020;10:20485.
66. Guo J et al. T follicular helper-like cells are involved in the pathogenesis of experimental autoimmune encephalomyelitis. *Front Immunol.* 2018;9:944.
67. Quinn JL, Kumar G, Agasing A, Ko RM, Axtell RC. Role of TFH cells in promoting T Helper 17-induced neuroinflammation. *Front Immunol.* 2018;9:382.
68. Wingerchuk DM et al. International consensus diagnostic criteria for neuromyelitis optica spectrum disorders. *Neurology.* 2015;85(5):177–189.
69. Luong TN, Carlisle HJ, Southwell A, Patterson PH. Assessment of motor balance and coordination in mice using the balance beam. *J Vis Exp.* 2011;49:2376.

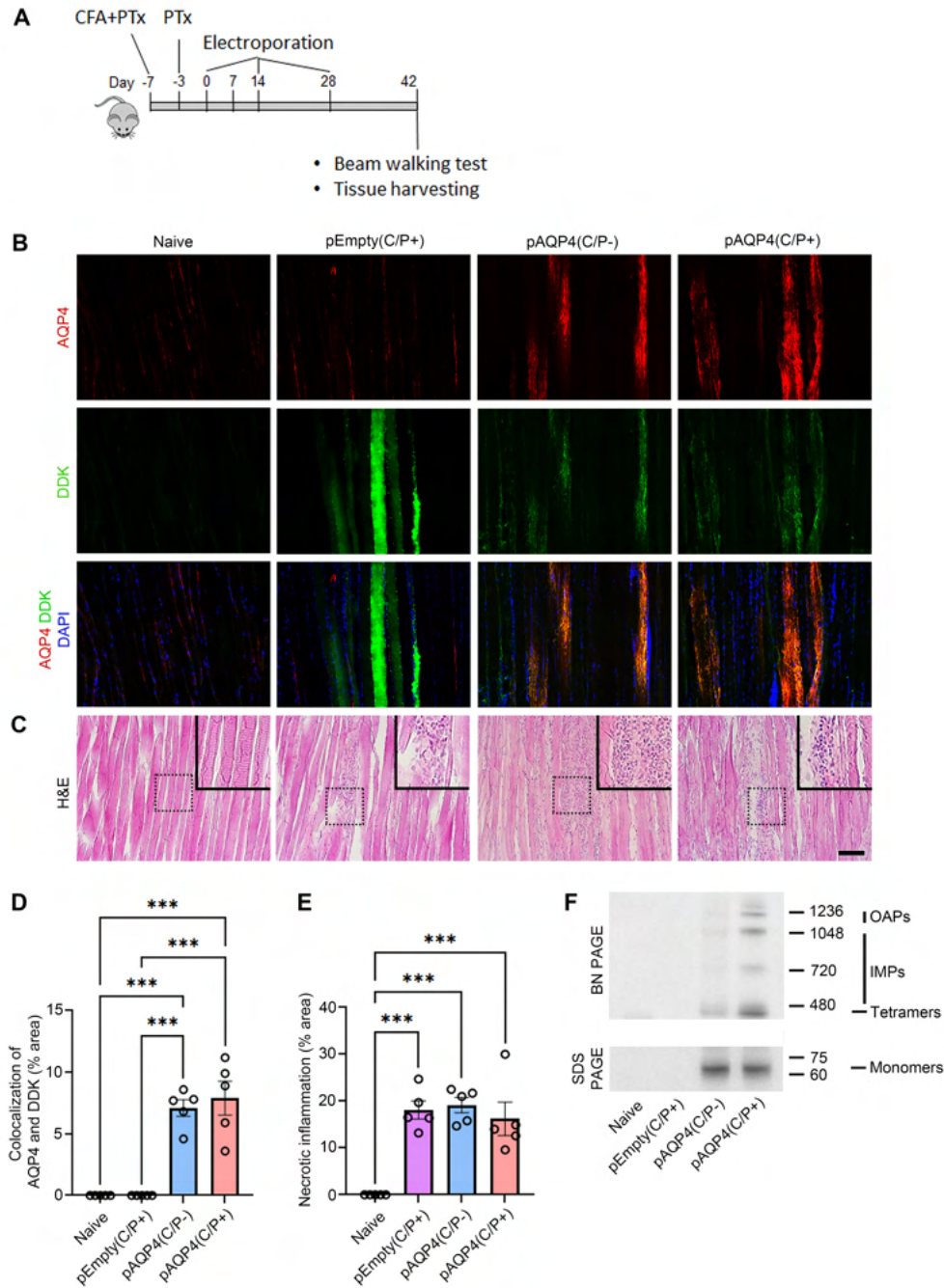


Figure 1. In vivo electroporation triggers AQP4 overexpression in skeletal muscle. (A) Experimental design. Mice were pre-treated with CFA and PTx. Then animals received in vivo electroporation of pAQP4 or pEmpty at the left tibialis anterior muscle. Electroporation was performed at day 0, 14 and 28. Animals were culled at day 42. **(B)** Co-immunostaining for AQP4 and Myc-DDK in skeletal muscle. Nuclei were counterstained with DAPI. **(C)** H&E staining for skeletal muscle. Images are representatives of the longitudinal section of

the tibialis anterior muscle from 5 mice per group. Insets are higher magnification photomicrographs showing immune cell infiltration. **(D)** Percentage area of AQP4 and Myc-DDK colocalization in the muscle. **(E)** Percentage area of necrotic inflammation in the muscle. **(F)** Western blot analysis of protein from skeletal muscle cell lysate separated in native form by BN-PAGE, and in denatured form by SDS-PAGE. Upper panel, BN-PAGE shows the expression of fusion proteins consisting of Myc-DDK and AQP4 OAPs, IMPs and tetramers in the muscle after electroporation with pAQP4. Lower panel, SDS-PAGE shows the expression of a fusion protein (60 kDa) consisting of Myc-DDK and AQP4 M23 monomers in the muscle after electroporation with pAQP4. Data are mean \pm SEM; n = 5 per group. *** $P < 0.001$, one-way ANOVA with post hoc Tukey's test. Scale bar, 50 μ m.

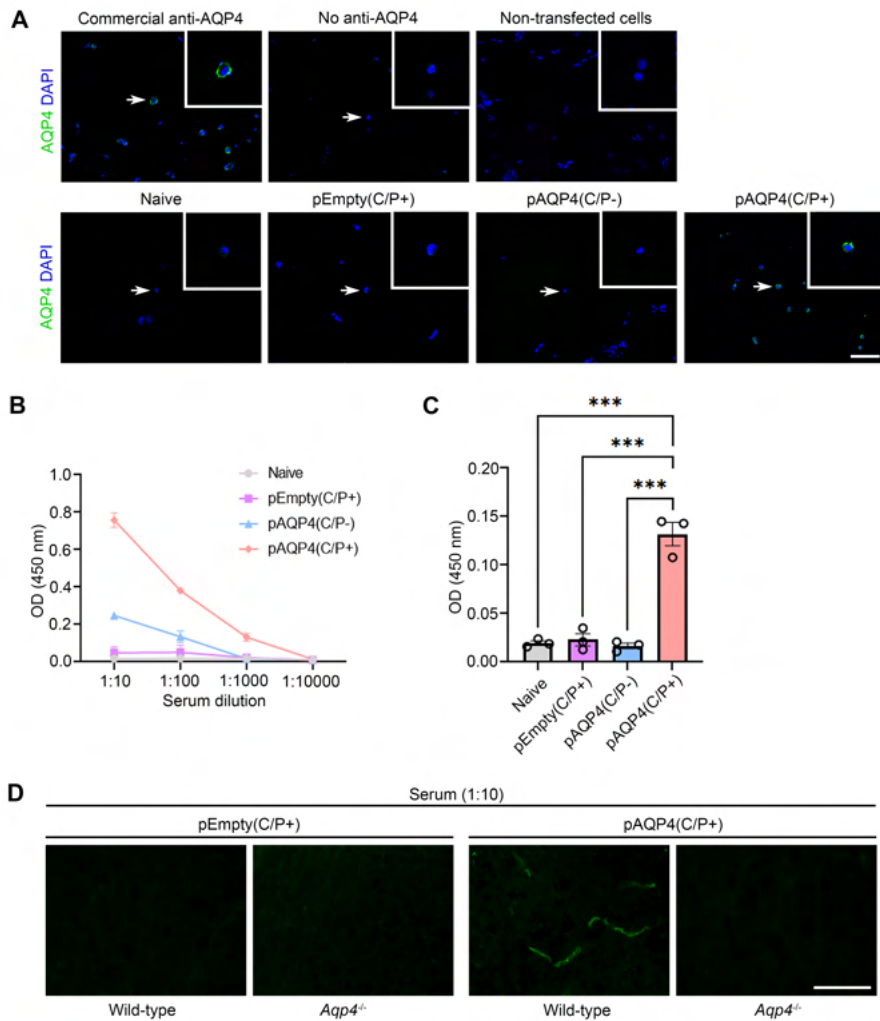


Figure 2. AQP4 immunization generates AQP4 autoantibodies. (A) Detection of AQP4 autoantibodies in mouse serum by cell-based indirect immunofluorescence assay. HEK293 cells were transfected with a plasmid encoding the mouse AQP4 M23 isoform. AQP4 autoantibodies in the serum were visualized by fluorescence-conjugated secondary antibody specific for mouse IgG. Upper left, immunostaining with commercial anti-AQP4 antibody revealed a discontinuous pattern of AQP4 staining on the cell membrane (positive control). Upper middle and right, no AQP4 immunoreactivity was observed when commercial anti-AQP4 antibody was absent or HEK293 cells were not transfected (negative controls). Lower panel, immunostaining of transfected HEK293 cells using the serum of naïve, pEmpty(C/P+), pAQP4(C/P-) and pAQP4(C/P+) mice. Nuclei were counterstained with DAPI. Images are representatives from 8 mice per group. (B) Titre of AQP4 autoantibodies was measured by

ELISA using serial dilution of serum from 1/10 to 1/10,000. (C) Concentration of AQP4 autoantibodies was determined using serum diluted at 1/1,000. (D) Spinal cord sections of wild-type and *Aqp4*-deficient (*Aqp4*^{-/-}) mice were immunostained using the serum of pEmpty(C/P+) and pAQP4(C/P+) mice. Images are representatives of 3 mice per group. Data are mean ± SEM; n = 3 per group. ****P* < 0.001, one-way ANOVA with post hoc Tukey's test. Scale bar, 50 μm.

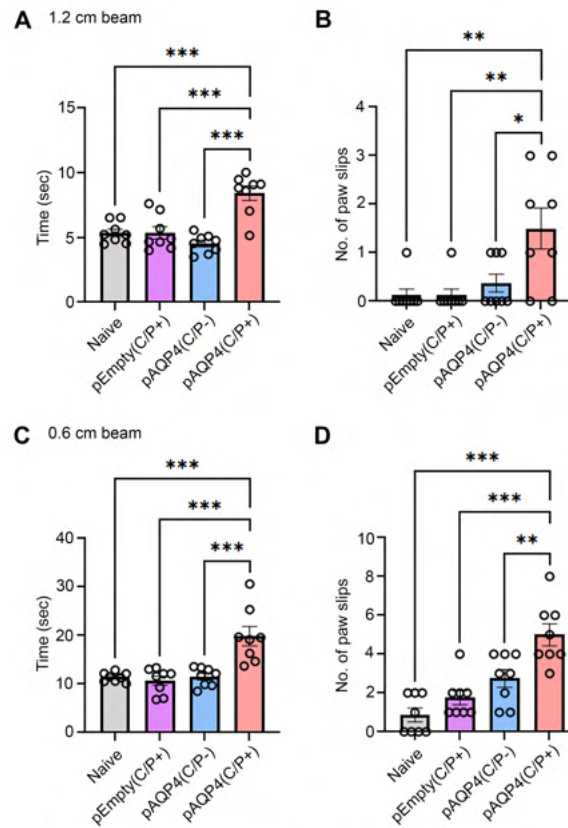


Figure 3. AQP4 immunization induces motor impairments. (A and B) Beam walking test measuring time taken for and number of paw slips while the mouse was crossing a 1.2 x 80 cm (width x length) beam. (C and D) Time taken for and number of paw slips while the mouse was crossing a 0.6 x 80 cm beam. Data are mean \pm SEM; n = 8 per group. *** P < 0.001, ** P < 0.01, * P < 0.05, one-way ANOVA with post hoc Tukey's test.

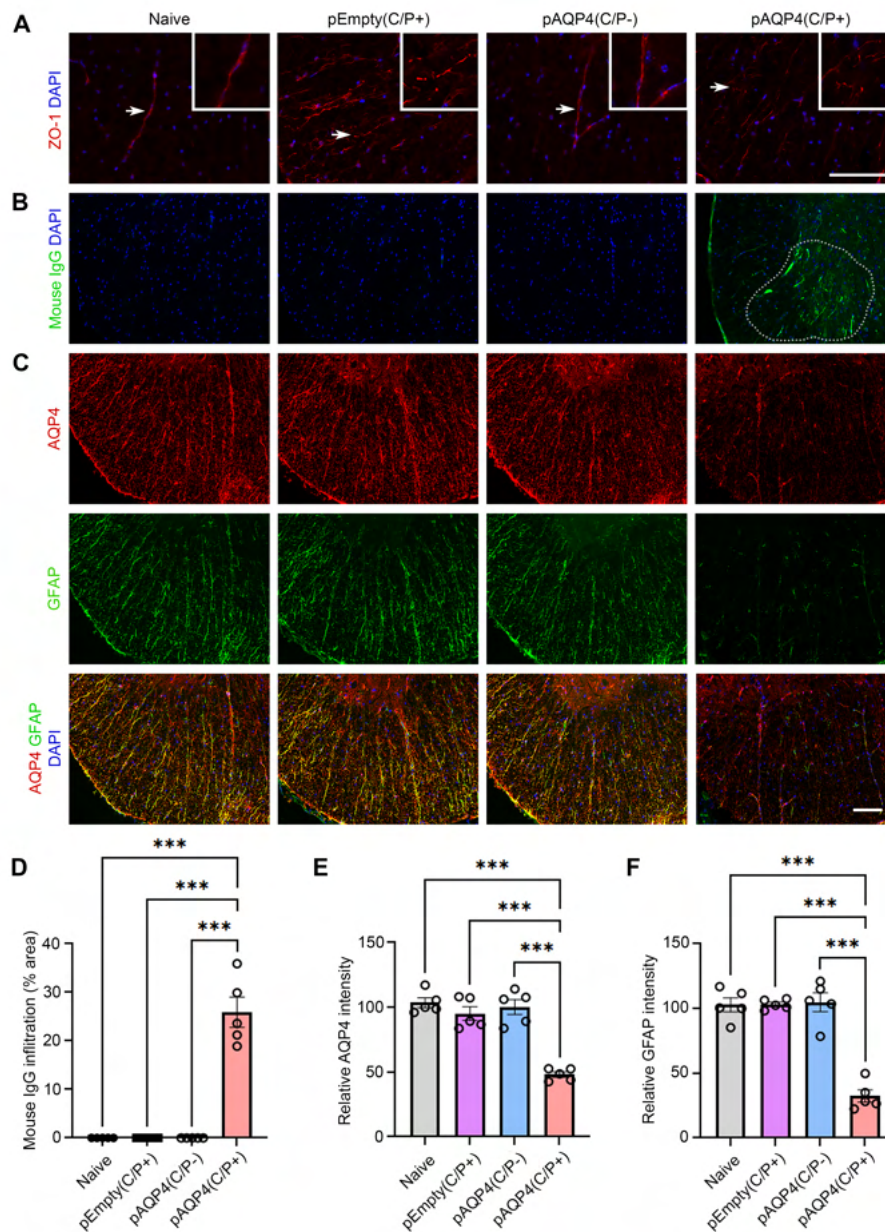


Figure 4. IgG infiltration and astrogliopathy after AQP4 immunization. (A)

Immunostaining for ZO-1 in the spinal cord of naïve, pEmpty(C/P+), pAQP4(C/P-) and pAQP4(C/P+) mice. Insets are higher magnification photomicrographs showing the pattern of ZO-1 staining in blood vessels. **(B)** Immunostaining for mouse IgG in the spinal cord of naïve, pEmpty(C/P+), pAQP4(C/P-) and pAQP4(C/P+) mice. Dotted line demarcates the area of mouse IgG immunoreactivity. **(C)** Co-immunostaining for AQP4 and GFAP in the spinal cord of naïve, pEmpty(C/P+), pAQP4(C/P-) and pAQP4(C/P+) mice. **(D)** Quantification of mouse IgG infiltration. **(E and F)** Quantification of AQP4 and GFAP immunofluorescence

intensities. Images are representative photomicrographs showing the ventrolateral white matter of cervical spinal cord cross sections from 5 mice per group. Nuclei were counterstained with DAPI. Scale bar, 50 μm . Data are mean \pm SEM; $n = 5$ per group. *** $P < 0.001$, one-way ANOVA with post hoc Tukey's test.

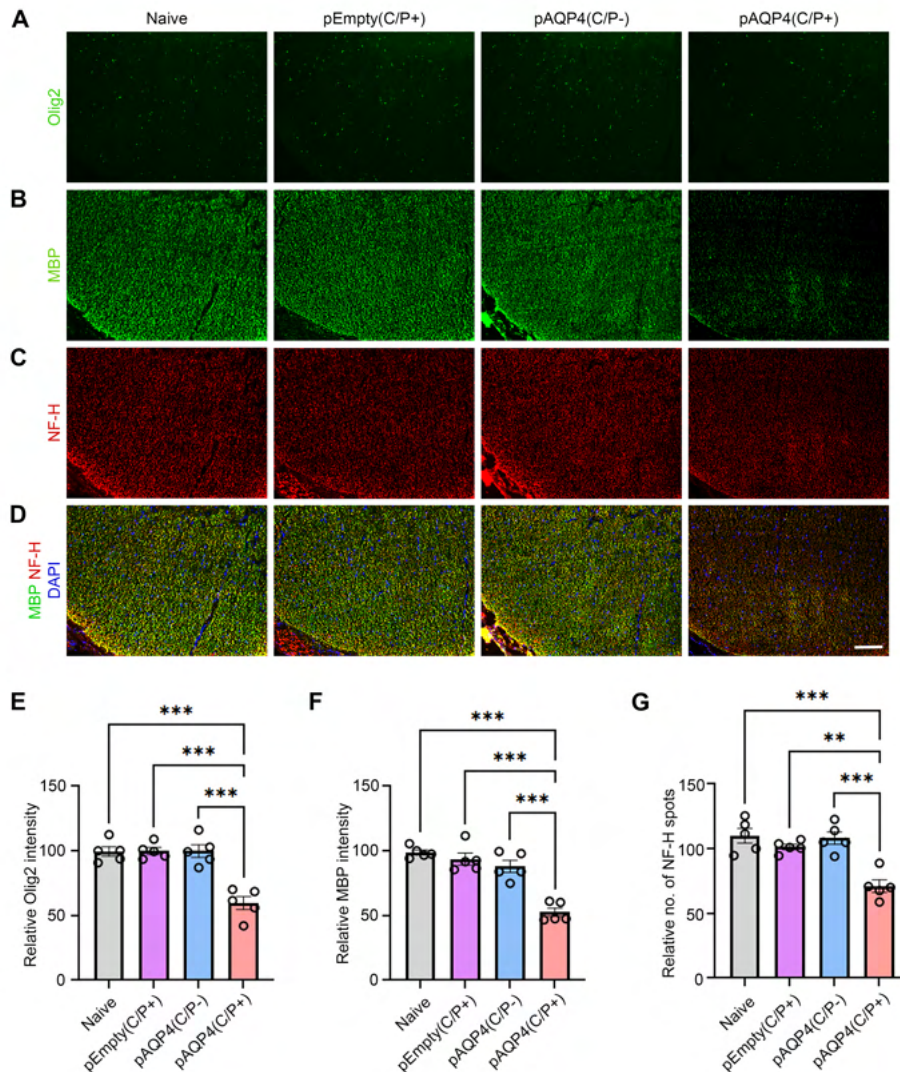


Figure 5. Oligodendrocyte loss, demyelination, and axonal loss after AQP4

immunization. (A-C) Immunostaining for Olig2 (A), MBP (B) and NF-H (C) in the spinal cord of naïve, pEmpty(C/P+), pAQP4(C/P-) and pAQP4(C/P+) mice. (D) Merged images of MBP and NF-H co-immunostaining. (E and F) Quantification of Olig2 and MBP immunofluorescence intensities respectively. (G) Quantification of the number of NF-H spots. Images are representative photomicrographs showing the ventrolateral white matter of cervical spinal cord cross sections from 5 mice per group. Nuclei were counterstained with DAPI. Scale bar, 50 μ m. Data are mean \pm SEM; n = 5 per group. *** $P < 0.001$, ** $P < 0.01$, one-way ANOVA with post hoc Tukey's test.

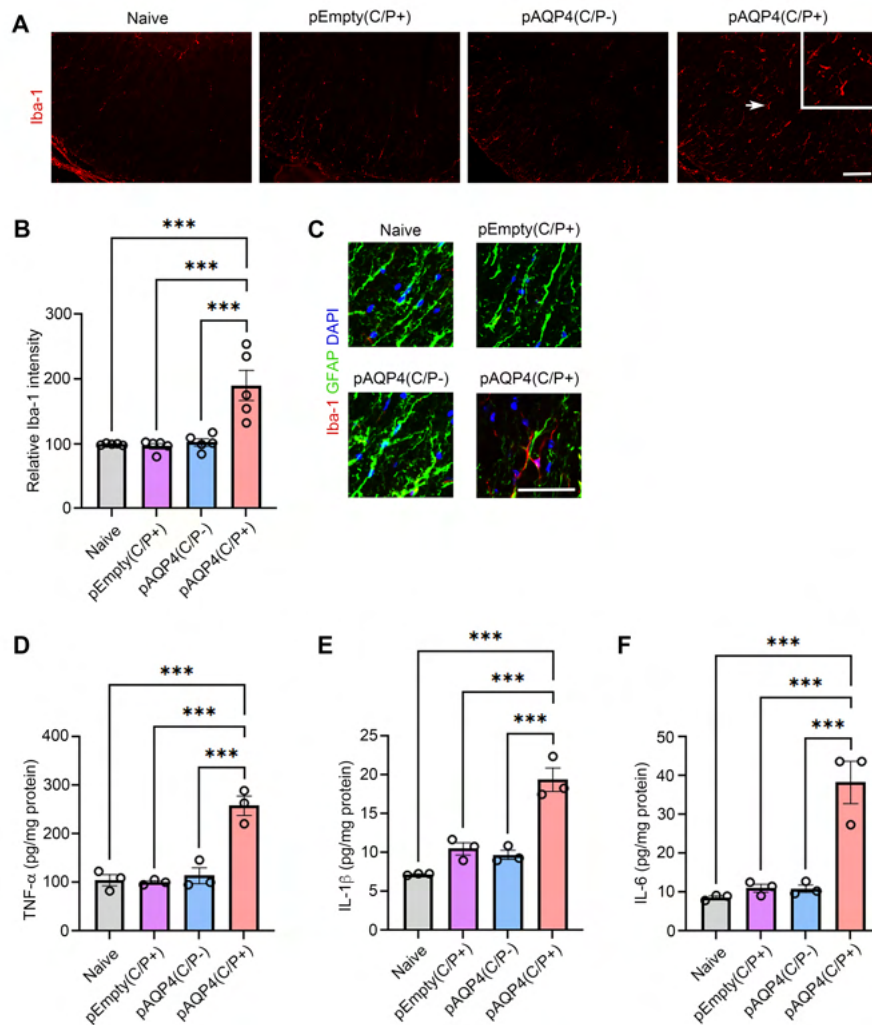


Figure 6. Microglia activation and increase in pro-inflammatory cytokine levels after AQP4 immunization. (A) Immunostaining for Iba-1 in the spinal cord of naïve, pEmpty(C/P+), pAQP4(C/P-) and pAQP4(C/P+) mice. (B) Quantification of Iba-1 immunofluorescence intensity. (C) Co-immunostaining for Iba-1 and GFAP. (D-F) ELISA of TNF- α , IL-1 β , and IL-6 levels in the spinal cord homogenate of naïve, pEmpty(C/P+), pAQP4(C/P-), and pAQP4(C/P+) mice. Images are representative photomicrographs showing the ventrolateral white matter of cervical spinal cord cross sections from 5 mice per group. Nuclei were counterstained with DAPI. Scale bar, 50 μ m. Data are mean \pm SEM; n = 5 per group (B), n = 3 per group (D-F). *** P < 0.001, one-way ANOVA with post hoc Tukey's test.

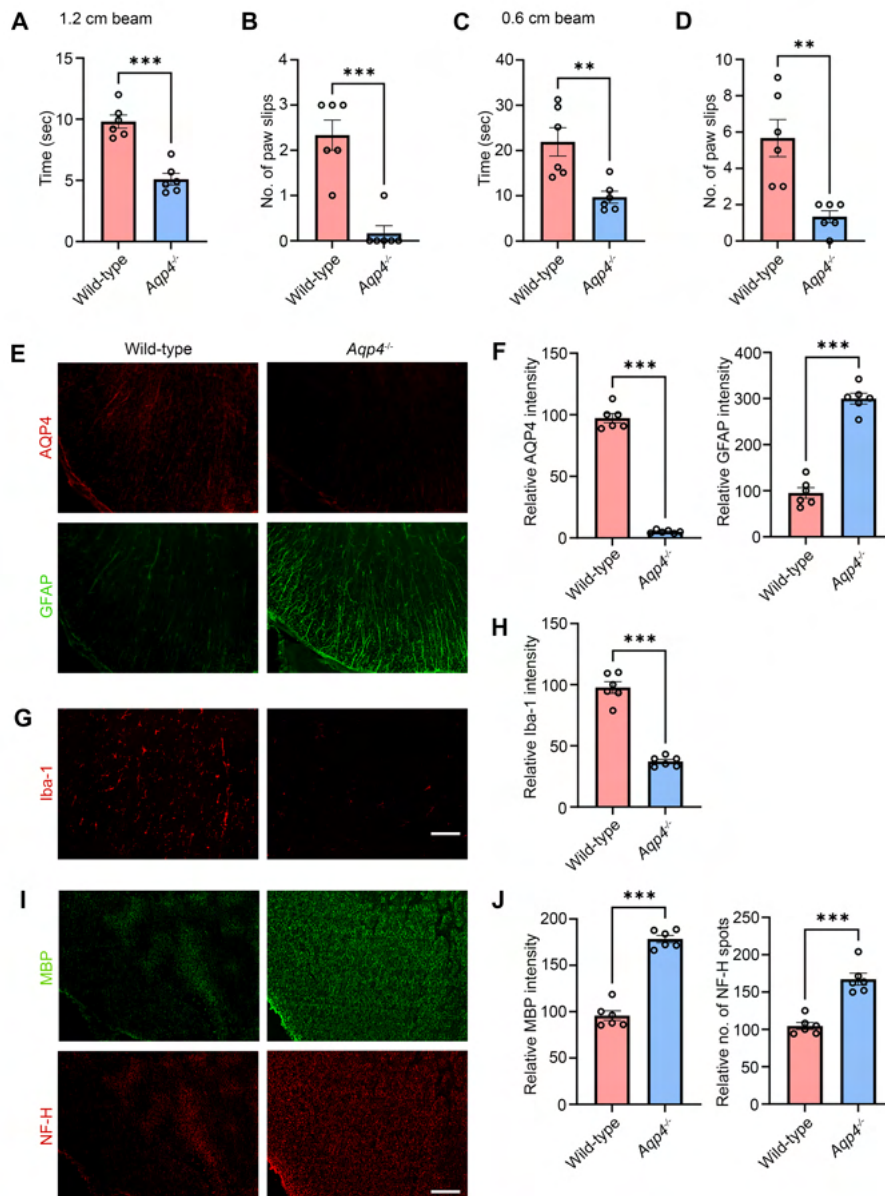


Figure 7. AQP4 immunization does not induce motor impairments and spinal cord pathologies in *Aqp4*-deficient mice. Wide-type or *Aqp4*-deficient (*Aqp4*^{-/-}) mice received in vivo electroporation of pAQP4 at the left tibialis anterior muscle. Electroporation was performed at day 0, 14 and 28. Animals were culled at day 42. **(A and B)** Beam walking test measuring the time taken for and the number of paw slips when the mouse was crossing a 1.2 x 80 cm (width x length) beam. **(C and D)** Time taken for and number of paw slips when the mouse was crossing a 0.6 x 80 cm beam. **(E)** Immunostaining for AQP4 and GFAP in the spinal cord of wild-type pAQP4(C/P+) and *Aqp4*^{-/-} pAQP4(C/P+) mice. **(F)** Quantification of

AQP4 and GFAP immunofluorescence intensities. (G) Immunostaining for Iba-1 in the spinal cord of wild-type pAQP4(C/P+) and *Aqp4*^{-/-} pAQP4(C/P+) mice. (H) Quantification of Iba-1 immunofluorescence intensity. (I) Immunostaining for MBP and NF-H in the spinal cord of wild-type pAQP4(C/P+) and *Aqp4*^{-/-} pAQP4(C/P+) mice. (J) Quantification of MBP immunofluorescence intensity and number of NF-H spots respectively. Images are representative photomicrographs showing the ventrolateral white matter of cervical spinal cord cross sections from 6 mice per group. Scale bar, 50 μm. Data are mean ± SEM; n = 6 per group. ****P* < 0.001, ***P* < 0.01, Student's *t* test.

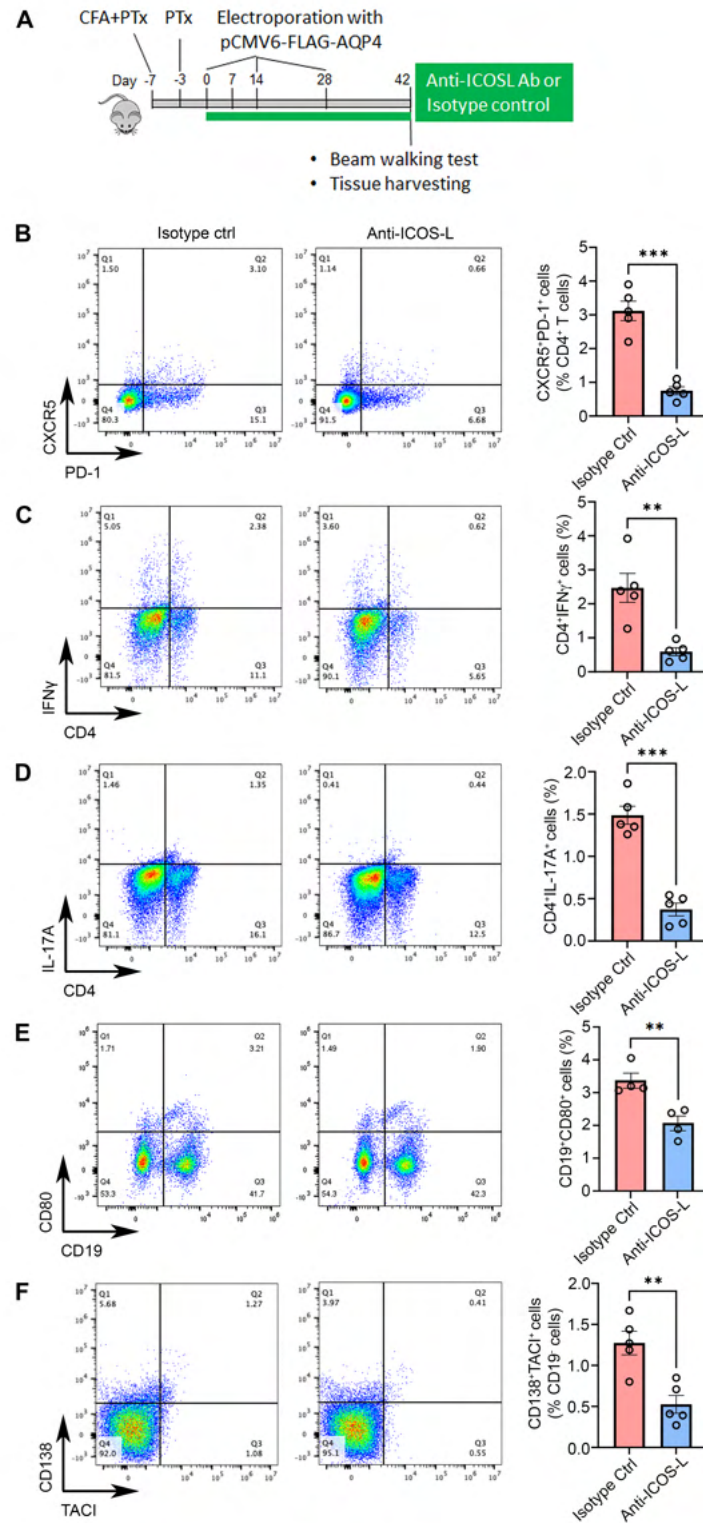


Figure 8. ICOS-L blockade depletes Tfh cells and suppresses Th1-, Th17-, memory B-, and plasma cell responses. (A) Experimental design. Beginning at day 0, pAQP4(C/P+) mice were administered 150 μ g anti-ICOS-L or isotype control antibody (i.p.) 3 times a week. Animals were culled at day 42. **(B)** Representative flow cytometry plots of splenic

CXCR5⁺PD-1⁺ Tfh cells following isotype control or anti-ICOS-L treatment, pre-gated on CD4⁺ T cells. (C) Representative flow cytometry plots of splenic CD4⁺IFN γ ⁺ Th1 cells following isotype control or anti-ICOS-L treatment. (D) Representative flow cytometry plots of splenic CD4⁺IL-17A⁺ Th17 cells following isotype control or anti-ICOS-L treatment. (E) Representative flow cytometry plots of splenic CD19⁺CD80⁺ memory B cells following isotype control or anti-ICOS-L treatment. (F) Representative flow cytometry plots of splenic CD138⁺TACI⁺ plasma cells following isotype control or anti-ICOS-L treatment, pre-gated on CD19⁻ cells. Flow data are quantified for all groups. Data are mean \pm SEM; n = 4 to 5 per group. *** $P < 0.001$, ** $P < 0.01$, Student's t test.

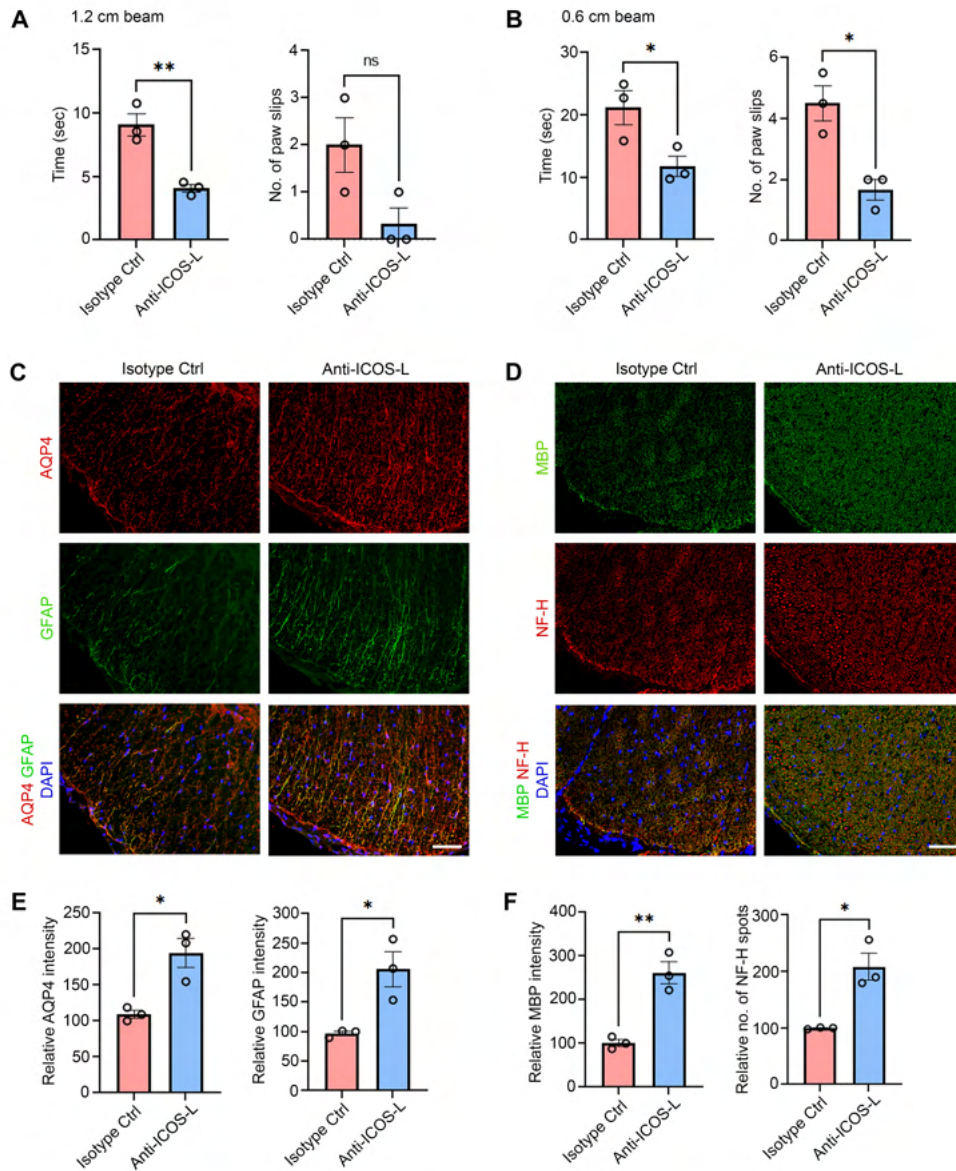


Figure 9. Tfh-cell depletion ameliorates NMO disease activity. Beginning at day 0, pAQP4(C/P+) mice were administered 150 μ g anti-ICOS-L or isotype control antibody (i.p) 3 times a week. Animals were culled at day 42. **(A and B)** Beam walking test measuring time taken for and number of paw slips while the mouse was crossing a 1.2 x 80 cm beam **(A)** and a 0.6 x 80 cm beam **(B)**. **(C)** Co-immunostaining for AQP4 and GFAP in the spinal cord of pAQP4(C/P+) mice following isotype control or anti-ICOS-L treatment. **(D)** Co-immunostaining for MBP and NF-H in the spinal cord of pAQP4(C/P+) mice following isotype control or anti-ICOS-L treatment. **(E)** Quantification of AQP4 and GFAP immunofluorescence intensities respectively. **(F)** Quantification of MBP

immunofluorescence intensity and number of NF-H spots respectively. Images are representative photomicrographs showing the ventrolateral white matter of cervical spinal cord cross sections from 3 mice per group. Nuclei were counterstained with DAPI. Scale bar, 50 μm . Data are mean \pm SEM; n = 3 per group. ** $P < 0.01$, * $P < 0.05$, ns, non-significant, Student's t test.